

Spectral–Spatial Adaptive Sparse Representation for Hyperspectral Image Denoising

Ting Lu, Shutao Li, *Senior Member, IEEE*, Leyuan Fang, *Member, IEEE*, Yi Ma, and Jón Atli Benediktsson, *Fellow, IEEE*

Abstract—In this paper, a novel spectral–spatial adaptive sparse representation (SSASR) method is proposed for hyperspectral image (HSI) denoising. The proposed SSASR method aims at improving noise-free estimation for noisy HSI by making full use of highly correlated spectral information and highly similar spatial information via sparse representation, which consists of the following three steps. First, according to spectral correlation across bands, the HSI is partitioned into several nonoverlapping band subsets. Each band subset contains multiple continuous bands with highly similar spectral characteristics. Then, within each band subset, shape-adaptive local regions consisting of spatially similar pixels are searched in spatial domain. This way, spectral–spatial similar pixels can be grouped. Finally, the highly correlated and similar spectral–spatial information in each group is effectively used via the joint sparse coding, in order to generate better noise-free estimation. The proposed SSASR method is evaluated by different objective metrics in both real and simulated experiments. The numerical and visual comparison results demonstrate the effectiveness and superiority of the proposed method.

Index Terms—Hyperspectral image (HSI) denoising, sparse representation (SR), spatial similarity, spectral correlation.

I. INTRODUCTION

HYPERSPECTRAL images (HSIs) can provide rich spectral–spatial information, which has drawn much attention in remote sensing applications, including land use analysis, pollution monitoring, wide-area reconnaissance, and field surveillance [1]–[3]. Unfortunately, hyperspectral imaging often suffers from annoying degradations caused by the existence of noise [4]–[6], which not only affects the visual impression but also influences some subsequent image processing, e.g., classification, unmixing, and target detection. Therefore, it is critical to develop effective denoising technique for the HSI.

In the literature, noise reduction for the HSI is an active area of research in the field of remote sensing, where the noise is generally considered to be additive and randomly distributed [7]–[10]. By regarding each band as one independent 2-D image, denoising techniques developed in dealing

with 2-D images, (e.g., wavelet-based methods [11], [12] and total-variance-based methods [13], [14]) can be utilized in a bandwise manner. However, the bandwise methods are only dependent on spatial information in each spectral band, which easily fail in restoring the spectral bands corrupted by serious noise.

Instead of processing the HSI in a band-by-band manner, researchers have paid much attention to consider the HSI as a whole entity and develop various multidimensional image restoration techniques [15]–[17]. Typically, multidimensional Wiener filtering (MWF) extends the classical 2-D Wiener filtering to the tensor model by using multilinear algebra tools [15]. However, annoying artifacts and oversmooth effects will be introduced by the MWF method in the case that signal subspace and noise subspace are difficult to be distinguished [18]. In addition, there are some more advanced multidimensional methods, including the genetic kernel Tucker decomposition [16] and adaptive 3-D filtering [17]. Since all the abundant signals (containing a large number of relative pixels) and the rare signals (containing only a few relative pixels) are processed together, these multidimensional methods easily lead the rare signals to be unexpectedly removed [19].

In addition, by introducing 3-D block to replace 2-D block, the nonlocal means denoising technique [20] has been extended to its 3-D versions, which can better deal with multidimensional data restoration problems. Qian and Ye [21] proposed the 3-D nonlocal sparse (3D-NLS) denoising method, in order to improve the denoising performance by applying sparse representation (SR) techniques to effectively utilize the high nonlocal self-similarity. The 3D-NLS method works well in restoring low-level noisy bands, but fails in dealing with seriously degraded spectral bands. Some other 3-D cube-based denoising methods, e.g., the video block matching 3-D filtering (VBM3D) [22] and the block matching 4-D filtering (BM4D) [23], have been proposed to denoise multidimensional data recently. The VBM3D is effective in the case that the noise statistics in all bands are the same, but is much less suitable if the noise levels vary across bands, which is the general case of the HSI. By contrast, the BM4D can achieve better performance by considering the variance of noise deviation across bands. The drawback of the 3-D block-based denoising methods is that high spectral redundancy in all the continuous spectral bands is not fully used; instead, only local spectral correlation between a few adjacent bands is considered.

Some recent denoising techniques focus on exploiting both spectral information and spatial information to improve image quality. Chen *et al.* [24] introduced an HSI denoising algorithm by integrating the principal component analysis (PCA) transform and the wavelet shrinkage in one framework. This method utilizes the Sendur and Selesnick's bivariate wavelet

Manuscript received February 17, 2015; revised June 9, 2015 and July 7, 2015; accepted July 8, 2015. This paper was supported in part by the National Natural Science Fund for Distinguished Young Scholars of China under Grant 61325007 and in part by the National Natural Science Foundation of China under Grant 61172161.

T. Lu, S. Li, and L. Fang are with the College of Electrical and Information Engineering, Hunan University, Changsha 410082, China (e-mail: tingluhnu@gmail.com; shutao_li@hnu.edu.cn; fangleyuan@gmail.com).

Y. Ma is with First Institute of Oceanography, State Oceanic Administration, Shandong 266003, China (e-mail: mayimail@fio.org.cn).

J. A. Benediktsson is with the Faculty of Electrical and Computer Engineering, University of Iceland, Reykjavik 101, Iceland (e-mail: benedikt@hi.is).

Color versions of one or more of the figures in this paper are available online at <http://ieeexplore.ieee.org>.

Digital Object Identifier 10.1109/TGRS.2015.2457614

[25] denoising in spectral view followed by 2-D dual-tree complex wavelet denoising [26] in spatial view in the PCA domain. Yuan *et al.* [27] denoised the HSIs twice by using the spectral or the spatial information separately and then fused both results according to the Q-metric [28]. Both HSI denoising methods proposed in [24] and [27] exploit the spectral and spatial information independently.

As one promising tool for image processing, the SR theory assumes that an image can be well approximated in terms of a linear combination of a few atoms in a dictionary. Traditionally, the SR can effectively exploit spatial self-similarity in an image, which can be easily developed to denoise HSI in a bandwise manner. However, the bandwise denoising approaches neglect the spectral correlation and continuity in HSI. To further exploit the spectral-spatial information to generate better noise-free estimation, some SR-based HSI denoising methods [24], [29] have been developed, by utilizing the wavelet-transformation-based fixed dictionary and performing a shrinkage operation over the coefficients. However, fixed dictionary is independent of the data being processed, which cannot adaptively represent the observed data. Therefore, the data-driven dictionary learning methods for the HSI are developed based on 3-D spatial-spectral blocks [21], [30]. The 3-D processing methods can effectively utilize the high nonlocal self-similarity in HSI, but they fail in dealing with serious noise. More recently, some advanced studies [31]–[33] have attempted to develop new denoising models for solving the HSI restoration problem, by adding the low-rank or nonnegativity constraints to the SR denoising models.

In this paper, the spectral-spatial adaptive sparse representation (SSASR) method is proposed for denoising HSI. By jointly exploiting the correlated spectral information and similar spatial information in HSI based on the SR, effective noise-free estimation can be generated by the SSASR. First, spectral-adaptive band-subset partition is introduced to group highly correlated spectral bands and separate low-correlated ones. In each band subset, the highly correlated spectral bands have continuous and close spectral characteristics. Second, spatial-adaptive similar pixel searching strategy is proposed to group similar pixels in local regions. In each spatial similar region, the pixels have closely spatial characteristics. Finally, an SR model is used to adaptively represent each group of highly spectral-correlated and spatial-similar pixels, resulting in the noise-free estimation. The denoising experiments conducted in both simulated and real HSI data sets demonstrate the effectiveness of the proposed method.

The rest of this paper is structured as follows. First, Section II briefly overviews the SR-based denoising method for 2-D images. Second, Section III introduces the proposed SSASR method for HSI denoising. Then, experimental results and analysis are reported in Section IV. Finally, conclusions and future work are given in Section V.

II. SR-BASED DENOISING FOR 2-D IMAGES

According to the SR theory, a noiseless signal can be modeled as a sparse linear combination of atoms selected from a given dictionary \mathbf{D} . Each image patch (with size of $\sqrt{n} \times \sqrt{n}$) extracted from the original image is lexicographically ordered as column vector, denoted by $\mathbf{y} \in R^n$. Then, the traditional

sparse coding can be modeled as an optimization problem [34], [35]

$$\hat{\alpha} = \arg \min_{\alpha} \|\mathbf{y} - \mathbf{D}\alpha\|_2^2 + \lambda \|\alpha\|_1 \quad (1)$$

where α is the estimated vector of sparse coefficient with respect to dictionary \mathbf{D} , and λ is the standard Lagrangian multiplier. Then, the noise-free estimation $\hat{\mathbf{x}}$ for vectored image patch \mathbf{y} can be calculated by

$$\hat{\mathbf{x}} = \mathbf{D}\hat{\alpha}. \quad (2)$$

A major drawback of the traditional sparse coding model in (1) is the independence assumption about sparsely coded patches. To further exploit nonlocal similarity in a degraded image, more advanced SR denoising methods simultaneously estimate each group of similar patches; the simultaneous sparse coding model introduced in [36] is given by

$$\hat{\mathbf{A}}_i = \arg \min \|\mathbf{Y}_i - \mathbf{D}\mathbf{A}_i\|_2^2 + \lambda \|\mathbf{A}_i\|_1 \quad (3)$$

where each column of \mathbf{Y}_i is one vectored image patch; correspondingly, each column of \mathbf{A}_i is the sparse coefficient vector.

III. SSASR METHOD FOR DENOISING HSI

Let $\mathbf{I} \in R^{M \times N \times B}$ represent one HSI, where $M \times N$ is the size of each spectral band, and B is the number of spectral bands. The commonly used image degradation model for each spectral band \mathbf{I}_i ($i \in [1, B]$) can be denoted by

$$\mathbf{I}_i = \mathbf{X}_i + \mathbf{N}_i \quad (4)$$

where \mathbf{X}_i and \mathbf{N}_i represent the clean and noisy components, respectively.

As shown in Fig. 1, the proposed SSASR method consists of three main stages: spectral-adaptive band-subset partition, spatial-adaptive local similar pixel searching, and SR-based noise-free estimation. First, according to the Pearson-correlation-coefficient-based metric, a coarse-to-fine band-subset partition is introduced to separate the HSI into multiple band subsets. Each band subset contains continuous spectral bands with high spectral correlation, whereas the correlation among spectral bands in different band subsets is low. Second, by applying the shape-adaptive (SA) local region searching on the weighted average generated fused image, local homogeneous region can be determined for each central spectral pixel. Each homogeneous region consists of multiple highly similar spectral pixels. Finally, by solving an SR-based optimization problem, the noise-free estimation for each group of spectral pixels with high spectral correlation and spatial similarity can be generated. Specifically, all the spectral pixels belonging to each group are vectorized to form a sparse matrix, which are jointly sparsely coded and reconstructed to generate the denoised estimation.

A. Spectral-Adaptive Band-Subset Partition

As one commonly used matrix correlation metric, the Pearson correlation coefficient is applied to assess the similarity between the spectral bands \mathbf{I}_i and \mathbf{I}_j , which is defined as

$$r(\mathbf{I}_i, \mathbf{I}_j) = \frac{\sum_{p=1}^{M \times N} (\mathbf{I}_{i,p} - \bar{\mathbf{I}}_i)(\mathbf{I}_{j,p} - \bar{\mathbf{I}}_j)}{\sqrt{\sum_{p=1}^{M \times N} (\mathbf{I}_{i,p} - \bar{\mathbf{I}}_i)^2 \cdot \sum_{p=1}^{M \times N} (\mathbf{I}_{j,p} - \bar{\mathbf{I}}_j)^2}} \quad (5)$$

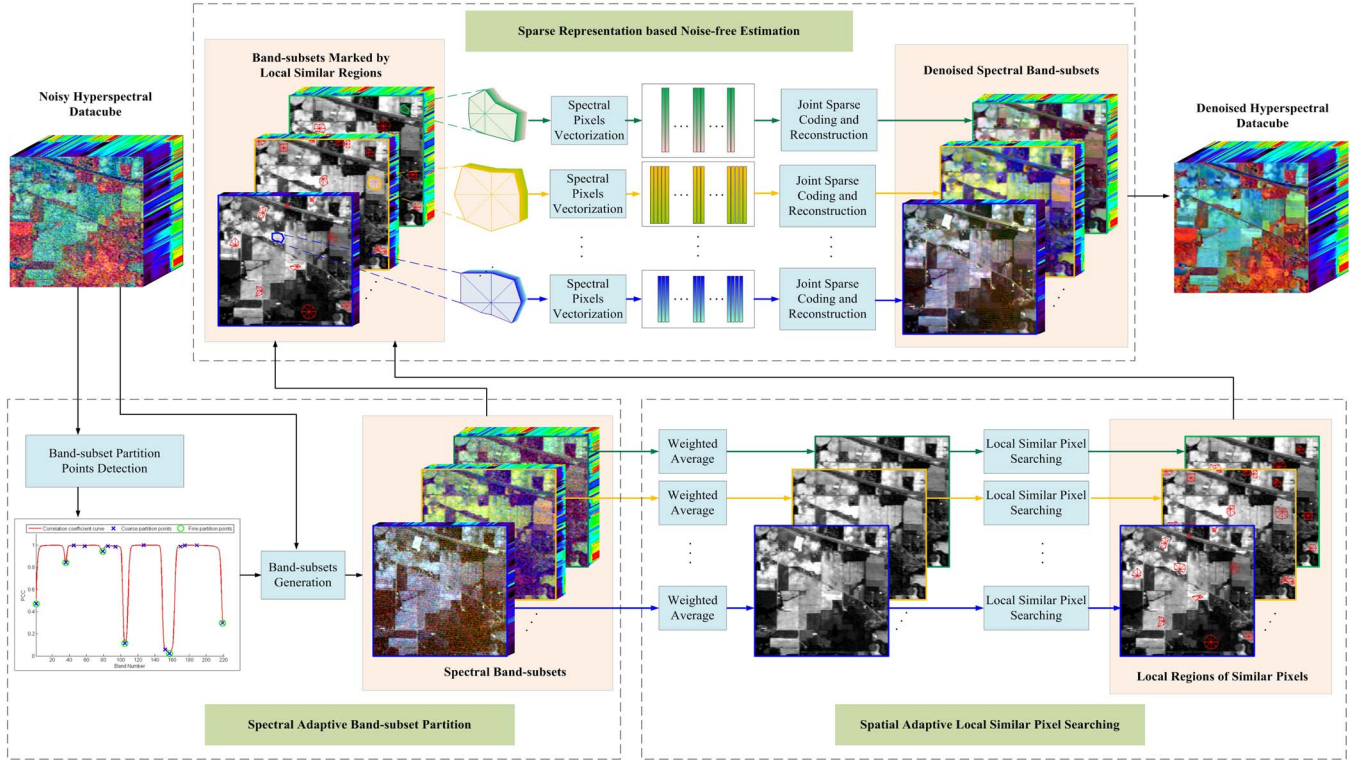


Fig. 1. Framework of the proposed SSASR method.

where $\bar{\mathbf{I}}_i$ ($\bar{\mathbf{I}}_j$) is the mean value of the spectral band \mathbf{I}_i (\mathbf{I}_j), and $\mathbf{I}_{i,p}$ ($\mathbf{I}_{j,p}$) represents the p th pixel in the i th (j th) spectral band. The closer $r(\mathbf{I}_i, \mathbf{I}_j)$ is to 1, the stronger the correlation is between the i th and j th spectral bands.

By applying (5) on adjacent spectral bands, a correlation curve C is generated, where $C(i) = r(\mathbf{I}_i, \mathbf{I}_{i+1})$. It can be seen from the red correlation coefficient curve in Fig. 1 (in the step of spectral-adaptive band-subset partition) that there are some sharp drops in curve C , whereas a relatively stable trend appears between two adjacent sharp drops. Therefore, the band-subset partition can be achieved based on detecting these sharp drops in curve C . The proposed coarse-to-fine band-subset partition mainly consists of the following two steps.

1) *Coarse Band-Subset Partition*: Local valley points are detected in the correlation coefficient curve C . If $C(i)$ meets the condition defined by

$$\begin{cases} C(i) - C(i-1) < 0 \\ C(i+1) - C(i) > 0 \end{cases} \quad (6)$$

then the i th point in the curve C is determined to be a local valley point, which can be regarded as one initial partition point. The spectral bands between two adjacent partition points are grouped to be one band subset $\mathbf{S}_q \in R^{M \times N \times B_q}$, where \mathbf{S}_q contains B_q spectral bands with a size of $M \times N$.

2) *Fine Band-Subset Partition*: To approximately represent spectral characteristics belonging to each \mathbf{S}_q , a weighted-average-based fused image $\bar{\mathbf{S}}_q$ is generated by performing weighted averaging on all the spectral bands as

$$\bar{\mathbf{S}}_q = \frac{1}{Z} \sum_{\mathbf{I}_i \in \mathbf{S}_q} w(\mathbf{I}_i) \mathbf{I}_i \quad (7)$$

where $Z = \sum_{\mathbf{I}_i \in \mathbf{S}_q} w(\mathbf{I}_i)$ is the normalizing constant, and the weight $w(\mathbf{I}_i)$ is defined according to the Gaussian kernel as

$$w(\mathbf{I}_i) = e^{-\left(\frac{\|\mathbf{I}_i - \mathbf{X}_i\|_2^2}{h^2}\right)}. \quad (8)$$

In (8), the item $\|\mathbf{I}_i - \mathbf{X}_i\|_2^2$ corresponds to the noise deviation σ_i^2 of noisy component \mathbf{N}_i , $\|\mathbf{I}_i - \mathbf{X}_i\|_2^2 = \sigma_i^2$, where σ_i can be estimated by the median-of-absolute-deviation-based method [37]. Therefore, by defining the weight in (8), the spectral bands with low image quality degradation can have a significant contribution on the fused image $\bar{\mathbf{S}}_q$. Based on (5) and (7), the correlation between band subsets \mathbf{S}_q and \mathbf{S}_{q+1} can be measured by $r(\bar{\mathbf{S}}_q, \bar{\mathbf{S}}_{q+1})$. Given a threshold T_r , band subsets \mathbf{S}_q and \mathbf{S}_{q+1} are determined to be merged in the condition of $r(\bar{\mathbf{S}}_q, \bar{\mathbf{S}}_{q+1}) > T_r$. In addition, considering a small band subset (i.e., a band subset with very few spectral bands) may not contain enough useful spectral information for an effective noiseless estimation, small band subsets are also merged with its neighboring subset. In practice, the band subset with less than five spectral bands is considered to be a small band subset.

B. Spatial-Adaptive Local Similar Pixel Searching

In the context of an HSI, a neighborhood region always has multiple pixels related to the same materials, which can be regarded as multiple observations for the same material. Based on this consideration, similar pixels in a local region are searched and jointly exploited to generate noiseless estimation. Specifically, a weighted-average-based fused image, denoted by $\bar{\mathbf{S}}_q$, is obtained by (7) first. Then, each local region containing spatially similar pixels is determined for each central pixel, $s \in \bar{\mathbf{S}}_q$, by applying the SA local region searching [38] on $\bar{\mathbf{S}}_q$, which is effective in finding a homogeneous region for each

pixel in the image. The SA algorithm is briefly described by the following two steps.

1) *Directional LPA-Based Filtered Estimation*: The 1-D local polynomial approximation (LPA) [39] kernel g is mathematically represented as $g = \mathbf{w}\Phi^{-1}[1\ 0\ 0, \dots, 0]^T$, where $\Phi = \phi^T \mathbf{w}\phi$, \mathbf{w} is a diagonal matrix of window function w , and ϕ is a vector of $m + 1$ polynomial functions. Let h and θ represent each of the varying scales and the varying directions, respectively. Foi *et al.* [38] developed the directional LPA kernel $g(h, \theta)$ in the 2-D domain by introducing varying scales and rotation transformation to the 1-D LPA kernel. In terms of varying scales and directions, a set of filtered estimations for $\hat{\mathbf{S}}_q$ can be generated by $\hat{\mathbf{S}}_q(h, \theta) = \bar{\mathbf{S}}_q \otimes g(h, \theta)$.

2) *ICI Rule Based Adaptive Selection*: For the i th specific scale h_i and the v th specific direction θ_v , let $\hat{s}(h_i, \theta_v) \in \hat{\mathbf{S}}_q(h_i, \theta_v)$ denote the filtered estimation for pixel s , and let F_i denote the confidence interval of estimation $\hat{s}(h_i, \theta_v)$; then, the intersection of confidence intervals (ICI) [40] between F_i ($i = \{1, j\}$) is represented as $I_j = \cap_{i=1}^j F_i$. For the case that $I_{j+} \neq \phi$ and $I_{j+1} = \phi$, h_{j+} is determined as the adaptive scale for s in the direction θ_v , represented as $h^+(s, \theta_v) = h_{j+}$. As shown in the local regions of similar pixels marked with the red polygons in Fig. 1 (in the step of spatial-adaptive local similar pixel searching), each searched SA region for each center pixel, i.e., s , is determined by $\{h^+(s, \theta_v)\}$ in terms of varying directions.

C. SR-Based Noise-Free Estimation

Based on the result of spectral-spatial similar pixel searching, each spectral pixel \mathbf{y}_i ($\mathbf{y}_i \in R^{B_q \times 1}$) in band subset \mathbf{S}_q corresponds to a local SA region. By ordering all the similar pixels in each SA region column by column, a matrix \mathbf{Y}_i can be formed. Since all the spectral pixels in \mathbf{Y}_i are highly similar, they should share a common sparsity pattern with different sets of coefficients, which can be modeled as a joint sparse coding problem in (3). The shape-adaptive iterative singular value thresholding algorithm (SAIST) [41], which can effectively solve (3) in an iterative way, is introduced and modified to deal with the problem of HSI denoising. For the $(k + 1)$ th iteration, the modified SAIST algorithm used for restoring each band subset \mathbf{S}_q is described as follows.

1) *Iterative Regularization*: The iterative regularization can be achieved by adding the filtered noise back to the denoised version, which has been demonstrated to be effective in improving the denoising performance [42], [43]. By considering that each spectral band is also one 2-D image, the iterative regularization can be introduced to the HSI in a band-by-band manner. Then, for each spectral band I_i , the regularization can be represented as $\mathbf{I}_i^{(k+(1/2))} = \hat{\mathbf{X}}_i^{(k)} + \gamma(\mathbf{I}_i - \hat{\mathbf{X}}_i^{(k)})$, where $\hat{\mathbf{X}}_i^{(k)}$ represents the noiseless estimation for \mathbf{I}_i in the k th iteration. Correspondingly, the updated band subset \mathbf{S}_q can be represented as

$$\hat{\mathbf{S}}_q^{(k+\frac{1}{2})} = \hat{\mathbf{S}}_q^{(k)} + \gamma(\mathbf{S}_q - \hat{\mathbf{S}}_q^{(k)}) \quad (9)$$

where $\hat{\mathbf{S}}_q^{(k)}$ denotes the noiseless estimation for \mathbf{S}_q in the k th iteration, and γ is a relaxation parameter.

2) *Update of the Noiseless Estimation for $\hat{\mathbf{Y}}_i$* : Each matrix $\mathbf{Y}_i^{(k)}$ is formed by vectorizing all the similar spectral pixels in a local SA region of the updated band subsets $\hat{\mathbf{S}}_q^{(k+(1/2))}$. As

shown in Fig. 1, the generation of each matrix \mathbf{Y}_i is illustrated in the step of the SR-based noise-free estimation. To adaptively characterize the similar pixels in $\mathbf{Y}_i^{(k)}$, the corresponding subdictionary \mathbf{D}_i can be constructed via the singular value decomposition (SVD) [41]. Specifically, the SVD is applied to decompose $\mathbf{Y}_i^{(k)}$ as (10). Then, the estimated subdictionary $\hat{\mathbf{D}}_i$ and the corresponding matrix of sparse coding coefficients $\hat{\mathbf{A}}_i$ can be given by (11). Thus

$$\mathbf{Y}_i^{(k)} = \mathbf{U}_i \Sigma_i \mathbf{V}_i^T \quad (10)$$

$$\hat{\mathbf{D}}_i = \mathbf{U}_i \quad \hat{\mathbf{A}}_i = S_\tau(\Sigma_i) \mathbf{V}_i^T \quad (11)$$

where S_τ is the shrinkage operator, and τ is a regularization parameter, which is updated during the iterative process of updating the noise-free estimation [41]. Correspondingly, the updated noiseless estimation for each matrix $\mathbf{Y}_i^{(k+1)}$ is

$$\hat{\mathbf{Y}}_i^{(k+1)} = \hat{\mathbf{D}}_i \hat{\mathbf{A}}_i. \quad (12)$$

Each column of $\hat{\mathbf{Y}}_i^{(k+1)}$ represents the updated noiseless estimation for the correlated spectral pixel.

3) *Update of the Noiseless Estimation for $\hat{\mathbf{S}}_q$* : Assuming the pixel \mathbf{y}_i is contained in J SA regions, then there are J noiseless estimations for \mathbf{y}_i , denoted by $\{\hat{\mathbf{y}}_{i,j}^{(k+1)}\}_{j=1}^J$. The denoised version for the i th pixel in $\hat{\mathbf{S}}_q^{(k+1)}$ is calculated by

$$\hat{\mathbf{S}}_q^{(k+1)}(i) = \frac{1}{J} \sum_{j=1}^J \hat{\mathbf{y}}_{i,j}^{(k+1)}. \quad (13)$$

By repeating steps 1–3 for T_{iter} times, the final noiseless estimation for each band subset can be generated.

IV. EXPERIMENTAL RESULTS AND DISCUSSIONS

A. Experimental Setup

Here, three hyperspectral data sets, including the ‘‘Washington DC Mall,’’ ‘‘AVIRIS Cuprite,’’ and ‘‘AVIRIS Indian Pines’’ [44], [45], are used for testing the denoising performance of the proposed method. In the section of parameter discussions, two subimages (191 bands, the size of each band is 256×256) of the data set Washington DC Mall are used. In the simulated experiments, another two subimages of Washington DC Mall and the data set of AVIRIS Cuprite (188 spectral bands, the size of each band is 250×191) are used. For the test data set of AVIRIS Cuprite, the 188 spectral bands with high signal-to-noise ratio (selected as in [46]) are remained as the noise-free reference. In the real data experiments, the data set of AVIRIS Indian Pines (220 bands, the size of each band is 145×145) is used. Before simulated and real experiments, the gray values of the test data sets are normalized to be values between $[0, 1]$. Based on the general case that the noise level varies across bands, zero-mean Gaussian noise in different degrees is added to each band in the simulated experiments, where the variance value σ is randomly selected between three ranges: $\sigma \in \{[0, 0.05], [0, 0.1], [0, 0.2]\}$.

In order to verify the effectiveness of the proposed SSASR method, it is compared with the wavelet-bishrink method [12] in a band-by-band manner, the BM4D method [23], and the PCA-wavelet [24] method. In addition, the denoising results by the proposed method with skipping the process of

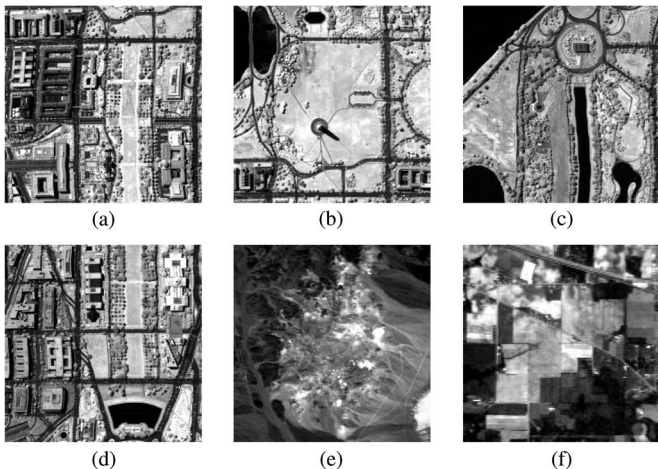


Fig. 2. Test data sets in both simulated and real experiments. (a)–(d) 60th spectral bands from four subimages of Washington DC Mall, with size of $256 \times 256 \times 191$. (e) Tenth spectral band from AVIRIS Cuprite, with size of $250 \times 256 \times 188$. (f) 18th spectral band from AVIRIS Indian Pines, with size of $145 \times 145 \times 220$. In the simulated experiments, (a) and (b) are used to test the influence of parameter T_r , which are named Test 1 and Test 2, respectively. (c) and (d) are used to compare the different HSI denoising methods, which are named “W-DC1” and “W-DC2,” respectively.

band-subset partition [named “spatial-adaptive sparse representation” (SASR)] are also compared, in order to demonstrate the necessity of the band-subset partition process. The execution code for the BM4D method can be obtained from [23]. In addition, the bandwise wavelet bishrink is achieved by applying the wavelet-shrinkage denoising band by band, where the noise standard deviation in each band is estimated by the median of absolute deviation technique [37]. Based on the description of the PCA-wavelet method in [24], both the pixelwise 1-D wavelet denoising and imagewise dual-tree complex wavelet denoising methods are applied in the PCA domain.

B. Parameter Discussion

The necessary parameters needed in the compared methods, including the wavelet-bishrink [12], BM4D [23], and PCA-wavelet [24] methods, are set to generate the best performance in terms of peak signal-to-noise ratio (PSNR) and structural similarity index metric (SSIM) [47] values. For the proposed SSASR method, two important parameters, namely, the threshold T_r in the stage of band-subset partition and the regularization parameter γ in (9), are discussed here in particular. As shown in Fig. 2(a) and (b), two subimages (named “Test 1” and “Test 2”) of the data set Washington DC Mall with nonoverlapping areas are tested. To objectively evaluate the influence of parameters T_r and γ on denoising results, the metrics of mean PSNR (MPSNR) and mean SSIM (MSSIM) are used. Let \hat{X}_i denote the denoised result for the i th spectral band I_i and B the number of the spectral bands in the tested HSIs. $\text{PSNR}(\hat{X}_i, I_i)$ and $\text{SSIM}(\hat{X}_i, I_i)$ are the calculated PSNR index and SSIM index of the i th denoised spectral band, respectively. Then, the MPSNR and the MSSIM are respectively calculated by

$$\text{MPSNR} = \frac{1}{B} \sum_{i=1}^B \text{PSNR}(\hat{X}_i, I_i) \quad (14)$$

$$\text{MSSIM} = \frac{1}{B} \sum_{i=1}^B \text{SSIM}(\hat{X}_i, I_i). \quad (15)$$

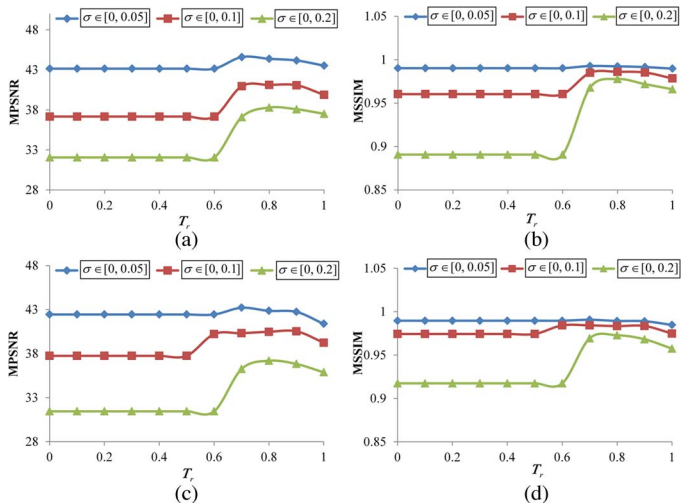


Fig. 3. Comparison of the denoising results with the parameter T_r ranging between $[0, 1]$. (a) MPSNR values of Test 1. (b) MSSIM values of Test 1. (c) MPSNR values of Test 2. (d) MSSIM values of Test 2.

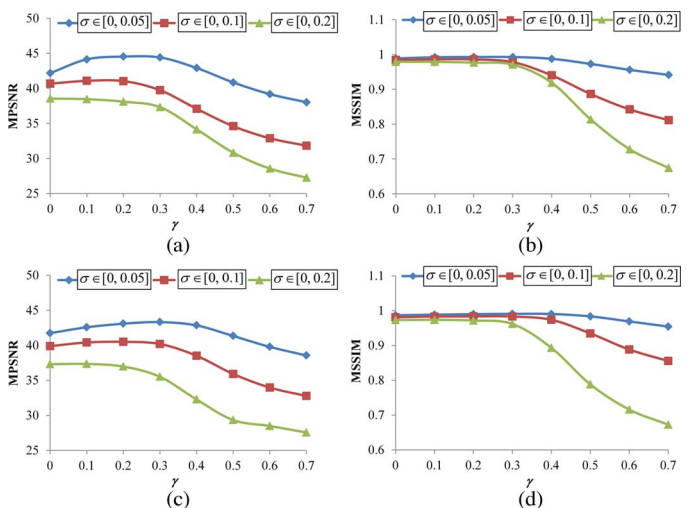


Fig. 4. Comparison of the denoising results with the parameter γ ranging between $[0, 0.7]$. (a) MPSNR values of Test 1. (b) MSSIM values of Test 1. (c) MPSNR values of Test 2. (d) MSSIM values of Test 2.

First, the influence of parameter T_r is tested by tuning T_r from 0 to 1. As shown in Fig. 3, it can be seen that the lowest MPSNR and MSSIM values are generated in the case of $T_r \in (0, 0.6)$. In fact, with T_r being below 0.6, all the spectral bands with low similarity are forced to be clustered into one band subset. By jointly processing the uncorrelated spectral bands with sparsity restriction, spectral distortion may be introduced. On the other hand, $T_r = 1$ means that the band-subset partition is only determined by the detected local valley points, easily resulting in that some band subsets may not have enough useful information to generate effective noise-free estimation. As T_r grows from 0.9 to 1, it can be seen that both the MPSNR and MSSIM values drop, demonstrating that too much high value of T_r affects the denoising performance in a negative way. By contrast, the peak MPSNR and MSSIM indexes can be obtained when $T_r \in (0.8, 0.9)$ according to Fig. 3. Therefore, T_r should be set to be values between $[0.8, 0.9]$ to generate the optimal denoised results. In the following simulated and real experiments, T_r is fixed to be 0.8.

TABLE I
MPSNR- AND MSSIM-BASED OBJECTIVE EVALUATION OF DIFFERENT DENOISING METHODS IN THE
SIMULATED EXPERIMENT WITH THE DATA SETS OF W-DC1, W-DC2, AND AVIRIS CUPRITE

		$\sigma \in [0, 0.05]$		$\sigma \in [0, 0.1]$		$\sigma \in [0, 0.2]$	
		MPSNR	MSSIM	MPSNR	MSSIM	MPSNR	MSSIM
W-DC1	Noisy Image	35.00	0.83	28.54	0.65	22.58	0.51
	Wavelet-bishrink [12]	35.73	0.93	31.94	0.86	28.05	0.75
	BM4D [23]	40.28	0.98	36.02	0.95	31.52	0.89
	PCA-wavelet [24]	41.69	0.99	38.35	0.97	34.15	0.93
	SASR	43.24	0.99	38.54	0.97	32.16	0.91
	SSASR	43.54	0.99	40.89	0.98	37.30	0.97
W-DC2	Noisy Image	35.16	0.86	29.19	0.71	23.59	0.45
	Wavelet-bishrink [12]	36.64	0.92	33.11	0.85	30.25	0.75
	BM4D [23]	40.87	0.98	36.63	0.94	32.29	0.85
	PCA-wavelet [24]	43.35	0.99	39.71	0.98	36.11	0.95
	SASR	44.33	0.99	37.84	0.95	32.64	0.86
	SSASR	46.23	0.99	42.70	0.99	38.75	0.97
AVIRIS Cuprite	Noisy Image	34.92	0.79	29.06	0.60	22.97	0.37
	Wavelet-bishrink [12]	37.09	0.90	34.16	0.84	31.31	0.75
	BM4D [23]	41.33	0.97	37.64	0.93	33.42	0.83
	PCA-wavelet [24]	43.59	0.98	39.50	0.96	35.46	0.92
	SASR	44.68	0.98	40.63	0.97	35.37	0.92
	SSASR	45.69	0.98	42.78	0.98	38.13	0.96

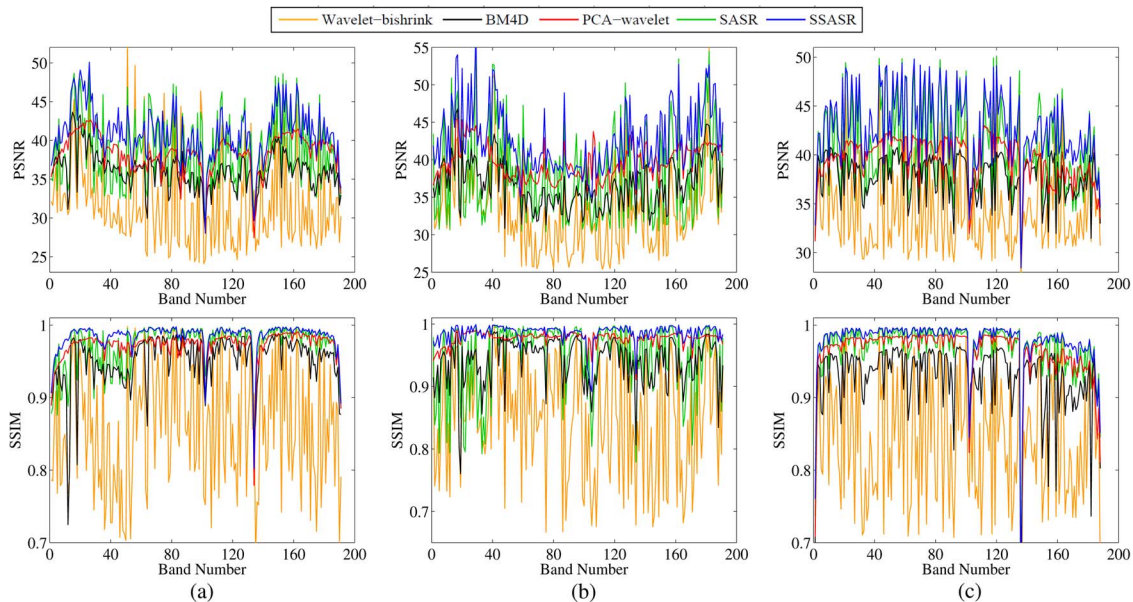


Fig. 5. Band-by-band PSNR and SSIM values of denoised spectral bands in the simulated experiments, noise of $\sigma \in (0, 0.1)$. (a) Test data set of W-DC1. (b) Test data set of W-DC2. (c) Test data set of AVIRIS Cuprite.

Then, the influence of the parameter γ , varying from 0 to 0.7, to the denoising performance in terms of the MPSNR and MSSIM values is shown in Fig. 4. In (9), the regularization parameter γ controls how much component of the filtered noise will be added to the updated denoised version, in order to decrease the loss of filtered useful component. It can be seen that both objective indexes decreased sharply as γ is getting larger than 0.3. This is because a much higher value of γ easily leads to the remained noisy component. In addition, it can be also seen that a much smaller value for γ (e.g., $\gamma = 0$) also negatively affects the denoising performance, particularly in the case of slight noise. This is because, without this regularization, oversmoothing effect is easy to be introduced. Based on the

overall observation in the PSNR and SSIM curves, stable and peak values can be achieved with $\gamma \in (0.1, 0.2)$. Therefore, the parameter γ is set to be 0.15 in all the experiments.

Apart from T_r and γ , some other necessary parameters are tuned to generate the best performance in terms of the PSNR and SSIM indexes. Specifically, the number of varying directions used to determine the local SA region is set to be 8, as suggested for the SA algorithm in [38]. Correspondingly, varying directions are represented as $\theta_k \in [0^\circ, 45^\circ, \dots, 315^\circ]$. The iteration time T_{iter} in generating the noise-free estimation is empirically set to be 12. The factor h in (8) is set to be the maximum value in $\{\sigma_i\}$, $\mathbf{I}_i \in \mathbf{S}_q$, in order to make sure all the weights $w(\mathbf{I}_i) \in [0, 1]$.

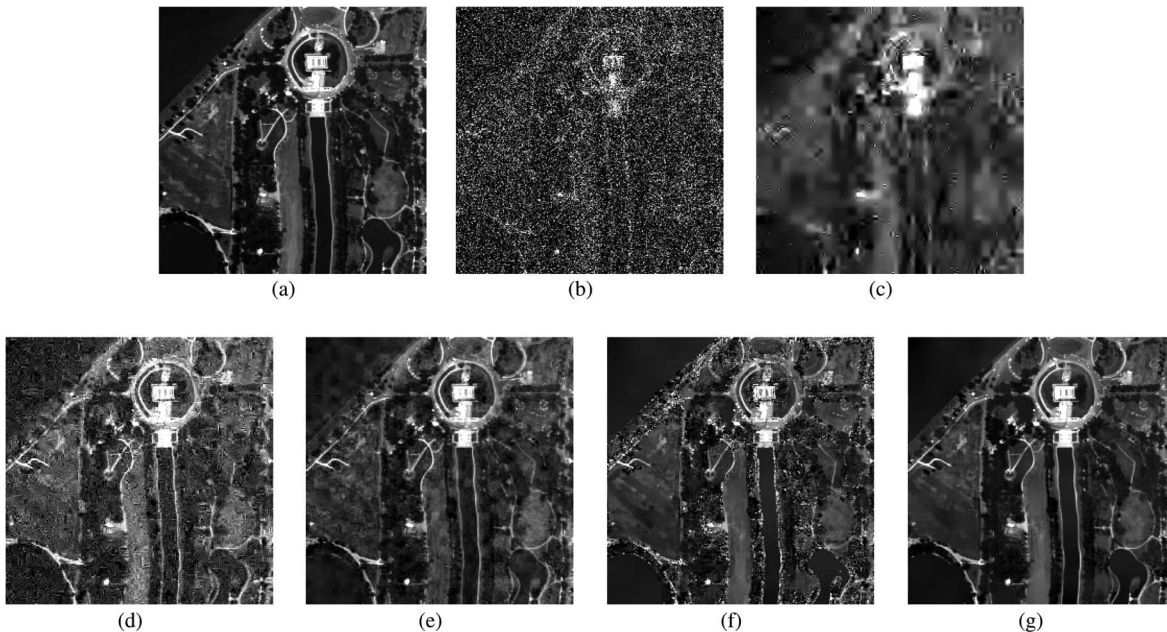


Fig. 6. Denoising results in simulated experiment with the data set of W-DC1. (a) Fourteenth spectral band in W-DC1. (b) Noisy spectral band with $\sigma \in [0, 0.2]$. (c) Wavelet-bishrink [12]. (d) BM4D [23]. (e) PCA-wavelet [24]. (f) SASR. (g) SSASR.

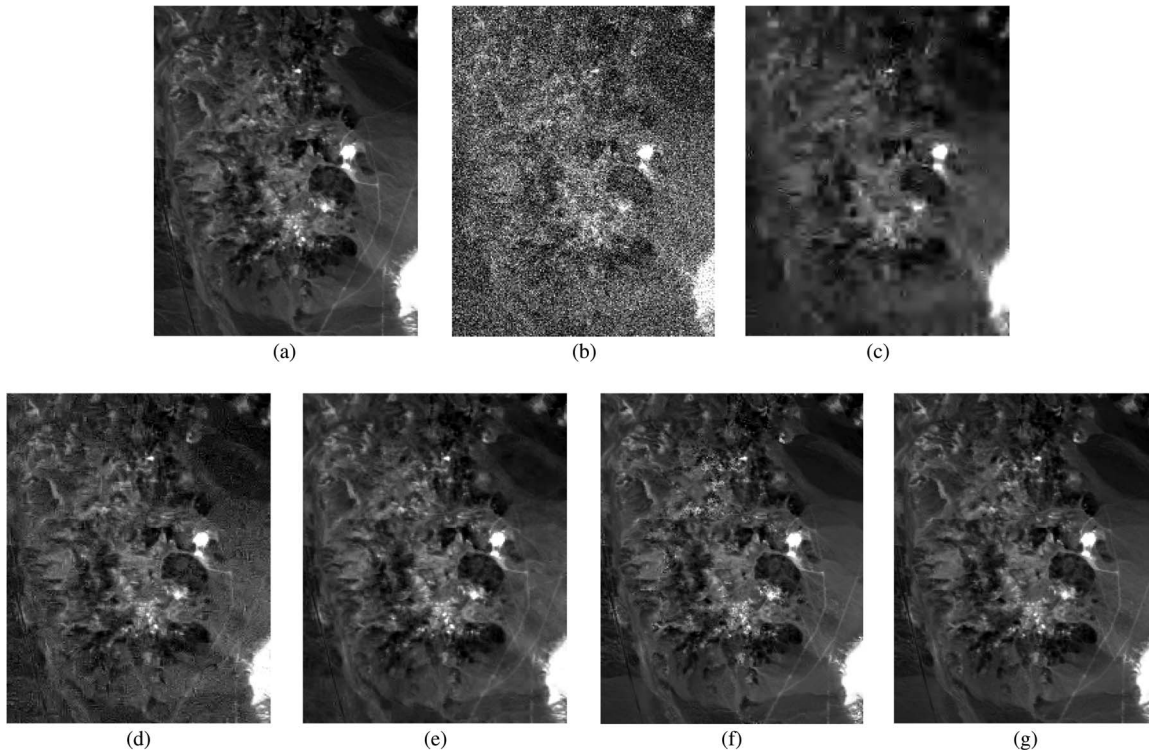


Fig. 7. Denoising results in simulated experiment with the data set of AVIRIS Cuprite. (a) One hundred fifty-ninth spectral band in AVIRIS Cuprite. (b) Noisy spectral band with $\sigma \in [0, 0.1]$. (c) Wavelet-bishrink [12]. (d) BM4D [23]. (e) PCA-wavelet [24]. (f) SASR. (g) SSASR.

C. Simulated Data Experiments

To compare the different HSI denoising methods, two sub-images of the data set Washington DC Mall [named W-DC1 and W-DC2; see Fig. 2(c) and (d)] and the data set AVIRIS Cuprite [see Fig. 2(e)] are tested. All the denoised results by different methods in comparison are evaluated from both the spatial and spectral viewpoints. From the spatial viewpoint, the objective indexes, i.e., PSNR and SSIM, are used

to give a quantitative assessment of the performance in the aspects of image quality improvement and structure preservation, respectively. In addition, visual comparisons of two denoised spectral bands, which are degraded by different degrees of noise, are also given. From the spectral viewpoint, both the spectral angle distance (SAD)-based and the Euclidean distance (ED)-based metrics are utilized. These two metrics have been commonly utilized in HSI domain to numerically evaluate the

TABLE II
MSAD- AND MED-BASED OBJECTIVE EVALUATION OF DIFFERENT DENOISING METHODS
IN THE SIMULATED EXPERIMENT WITH THE DATA SETS OF W-DC1 AND W-DC2

	$\sigma \in [0, 0.05]$		$\sigma \in [0, 0.1]$		$\sigma \in [0, 0.2]$	
	MSAD	Std-SAD	MSAD	Std-SAD	MSAD	Std-SAD
Noisy Image	0.126	0.088	0.244	0.152	0.440	0.220
Wavelet-bishrink [12]	0.072	0.039	0.107	0.057	0.150	0.082
BM4D [23]	0.040	0.020	0.064	0.033	0.109	0.057
PCA-wavelet [24]	0.031	0.021	0.046	0.030	0.072	0.052
SASR	0.030	0.019	0.055	0.036	0.105	0.079
SSASR	0.027	0.018	0.037	0.021	0.054	0.029
	MED	Std-ED	MED	Std-ED	MED	Std-ED
Noisy Image	0.155	0.021	0.627	0.088	2.530	0.370
Wavelet-bishrink [12]	0.080	0.069	0.191	0.190	0.420	0.476
BM4D [23]	0.021	0.011	0.054	0.033	0.158	0.102
PCA-wavelet [24]	0.013	0.070	0.029	0.121	0.072	0.158
SASR	0.012	0.011	0.051	0.064	0.219	0.298
SSASR	0.010	0.008	0.019	0.016	0.042	0.040

TABLE III
MSAD- AND MED-BASED OBJECTIVE EVALUATION OF DIFFERENT DENOISING METHODS
IN THE SIMULATED EXPERIMENT WITH THE DATA SET OF AVIRIS CUPRITE

	$\sigma \in [0, 0.05]$		$\sigma \in [0, 0.1]$		$\sigma \in [0, 0.2]$	
	MSAD	Std-SAD	MSAD	Std-SAD	MSAD	Std-SAD
Noisy Image	0.119	0.050	0.222	0.086	0.423	0.138
Wavelet-bishrink [12]	0.054	0.024	0.070	0.032	0.092	0.041
BM4D [23]	0.035	0.015	0.051	0.021	0.089	0.037
PCA-wavelet [24]	0.030	0.013	0.043	0.020	0.060	0.031
SASR	0.028	0.013	0.041	0.024	0.072	0.050
SSASR	0.026	0.012	0.034	0.016	0.054	0.031
	MED	Std-ED	MED	Std-ED	MED	Std-ED
Noisy Image	0.158	0.022	0.578	0.083	2.380	0.334
Wavelet-bishrink [12]	0.054	0.046	0.100	0.107	0.193	0.257
BM4D [23]	0.017	0.007	0.038	0.019	0.118	0.061
PCA-wavelet [24]	0.012	0.007	0.026	0.017	0.059	0.049
SASR	0.011	0.009	0.027	0.039	0.098	0.177
SSASR	0.009	0.004	0.015	0.011	0.045	0.050

similarity between spectral pixels [7], [27], [48]. The SAD and the ED are respectively calculated by

$$\text{SAD} = \cos^{-1} \left(\frac{\mathbf{s}_o^T \cdot \mathbf{s}_d}{\|\mathbf{s}_o\| \cdot \|\mathbf{s}_d\|} \right) \quad (16)$$

$$\text{ED} = (\mathbf{s}_o - \mathbf{s}_d)^T \cdot (\mathbf{s}_o - \mathbf{s}_d) \quad (17)$$

where \mathbf{s}_o and \mathbf{s}_d represent the original and denoised spectral pixels, respectively. Generally, the smaller the SAD and ED values are, the higher the similarity is between the spectral pixels \mathbf{s}_o and \mathbf{s}_d .

In Table I, the MPSNR and MSSIM values of all the denoised spectral bands are shown. It can be noticed that the lowest objective index values are generated by the wavelet-shrink [12] method. By exploiting the nonlocal similarity and adaptively adjusting the denoising strength in each spectral band, BM4D [23] demonstrates a better denoising performance than the band-by-band wavelet bishrink, whereas obvious gains can be observed in both the PCA-wavelet [24] and SSASR methods. Overall, the consistently highest MPSNR values obtained by the SSASR method demonstrate the superiority over the other compared methods in improving the overall image quality. In addition, the relatively stable and high MSSIM values (varying from 0.96 to 0.99) in dealing with different degrees of noise

demonstrate the excellent performance in terms of structure preservation. Furthermore, it is clear that there is an obvious rise in the values of the objective indexes when the SSASR method is compared with the SASR method, which illustrates that processing the whole HSI in a band-subset-based manner greatly improves the denoising performance, owing to the better utilization of high spectral correlation.

Fig. 5 shows the band-by-band PSNR and SSIM values of the denoised results in the case of $\sigma \in (0, 0.1)$, in order to compare the denoising performance of different methods in processing each spectral band of the HSI. In line with the objective indexes shown in Table I, the wavelet-bishrink method results in the lowest PSNR and SSIM values, exhibiting much worse denoising capability than the other compared methods. In addition, the BM4D method exhibits quite unstable performance in processing different spectral bands with various degrees of noise. When compared with the SASR method, the SSASR method has better stability in terms of PSNR- and SSIM-based metrics. Although the PCA-wavelet method also has a relatively stable capability in dealing with different spectral bands, obvious increase in the PSNR and SSIM values of the majority of spectral bands indicates that the proposed SSASR method can generate denoised result with better image quality.

To visually compare the denoising results by different methods, Figs. 6 and 7 show the denoised results for two spectral bands from the data sets of Washington DC Mall and AVIRIS Cuprite. In Fig. 6, the denoised results of the noisy 14th spectral band in W-DC1 (the noise deviation $\sigma \in (0, 0.2)$) are shown. The original noise-free reference image and the simulated noise-corrupted image are shown in Fig. 6(a) and (b), respectively. Since this spectral band is corrupted by serious noise, the bandwise wavelet-shrink method fails to restore the details effectively. Although the BM4D, PCA-wavelet, and SASR methods can recover more structure and details, either obvious artifacts or remained noise can be observed in the denoised results. In contrast, the noise-free estimation generated by the proposed SSASR method has better visual impression, with sharper edges and smoother flat regions.

In Fig. 7, another set of visual comparison results for the 159th spectral band in the AVIRIS Cuprite (the noise deviation $\sigma \in (0, 0.1)$) is shown. Without exploiting the highly correlated spectral information, the bandwise wavelet-bishrink method processes each spectral band separately, resulting in a serious oversmoothing effect. Similarly, BM4D cannot avoid the loss of details in most areas and the introduction of artifacts. In contrast, the PCA-wavelet method can preserve details better, but blurring effect can be noticed around edges. In the proposed SSASR method, both highly correlated spectral information and highly similar spatial information are effectively utilized via the SR to improve the denoising results. Consequently, a good balance between smoothing and structure preservation can be achieved, as shown in Fig. 7(g). Meanwhile, no obvious annoying artifacts are introduced by the SSASR method.

In addition to the spatial comparison results, the SAD and ED metrics are introduced to measure the performance of different methods in preserving spectral characteristics. In practice, all the SAD and ED values between the original spectral signals and the corresponding denoised ones are calculated in a pixel-by-pixel manner. The total number of spectral signals is so huge that it is not appropriate to demonstrate performance measured on a pixel-by-pixel basis. Instead, as shown in Tables II and III, the mean values of all the SAD and ED values for the simulated data sets W-DC1, W-DC2, and AVIRIS Cuprite (denoted by MSAD and MED, respectively) are given. Meanwhile, the standard deviations of all the SAD and ED values (denoted by Std-SAD and Std-ED, respectively) are also calculated to illustrate the stability of the objective indexes. In terms of both SAD- and ED-based objective metrics, it is clear that both the BM4D and PCA-wavelet methods have better performance than the wavelet-bishrink method, but still inferior when compared with the proposed SSASR method. In addition, although the SASR method generates very competitive results in the condition of $\sigma \in (0, 0.05)$, the performance is sharply decreased as σ increases to values higher than 0.1, particularly for the data sets of W-DC1 and W-DC2. Overall, the consistent lowest MSAD and MED values and the quite low Std-SAD and Std-ED indexes obtained by the SSASR method demonstrate the effectiveness and merit of the proposed method in preserving spectral characteristics.

D. Real HSI Data Experiments

In the real HSI data experiment, the data set of AVIRIS Indian Pines is used, as shown in Fig. 2(f). In this data set, some

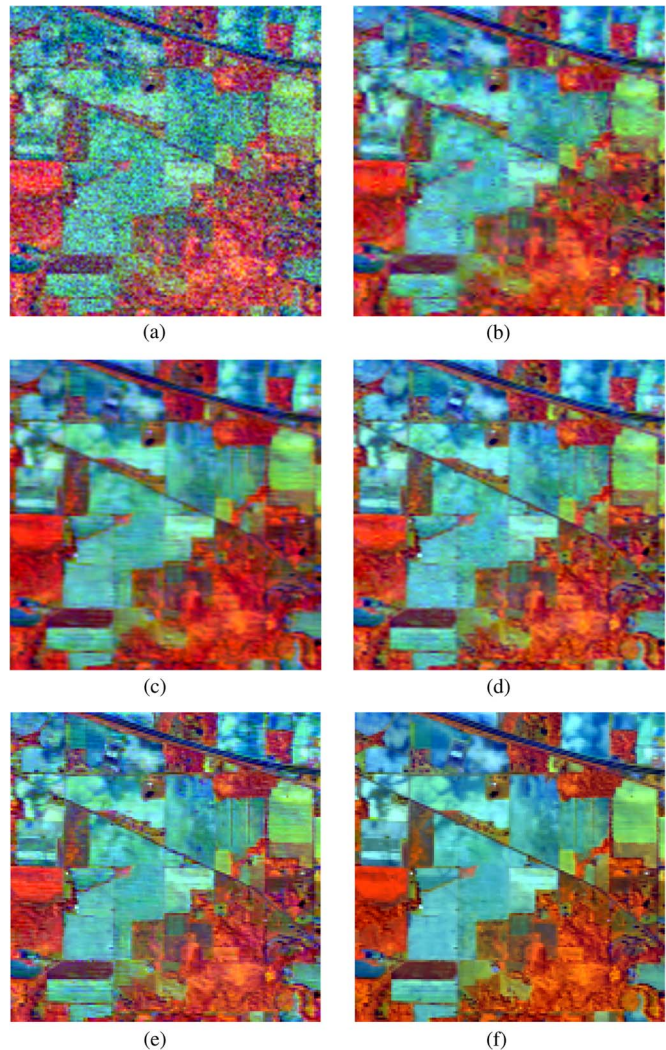


Fig. 8. Denoising results of the 54th, 103rd, and 219th spectral bands in the data set of AVIRIS Indian Pines. (a) Original spectral bands. (b) Wavelet-bishrink [12]. (c) BM4D [23]. (d) PCA-wavelet [24]. (e) SASR. (f) SSASR.

spectral bands are strongly degraded, whereas some other ones are slightly noisy.

Figs. 8 and 9 visually show denoised results for different spectral bands, which are corrupted by varying degrees of noise. In Fig. 8(a), the noisy three-channel image is composed of the 54th, 103rd, and 219th bands. It can be seen that the image quality of the denoised results by the wavelet-bishrink approach is greatly improved when it is compared with the original noisy ones, but an obvious oversmoothing effect and loss of details can be noticed in Fig. 8(b). BM4D has a much better visual impression, except for the obvious stripping effect and oversmoothing in Fig. 8(c). In contrast, the PCA-wavelet, SASR, and SSASR methods have a better balance between smoothing and structure preservation. However, by taking a closer look at Fig. 8, it can be seen that the edges obtained by the proposed SSASR method are sharper than the results by the compared methods.

In addition, Fig. 9 shows five groups of denoising results of the 1st, 25th, 79th, 108th, and 163rd spectral bands, which are corrupted by varying degrees of noise. In the condition of very slight noise (e.g., the 25th and 79th spectral bands), the performances of both the compared methods and the proposed SSASR method are competitive in terms of smoothing flat

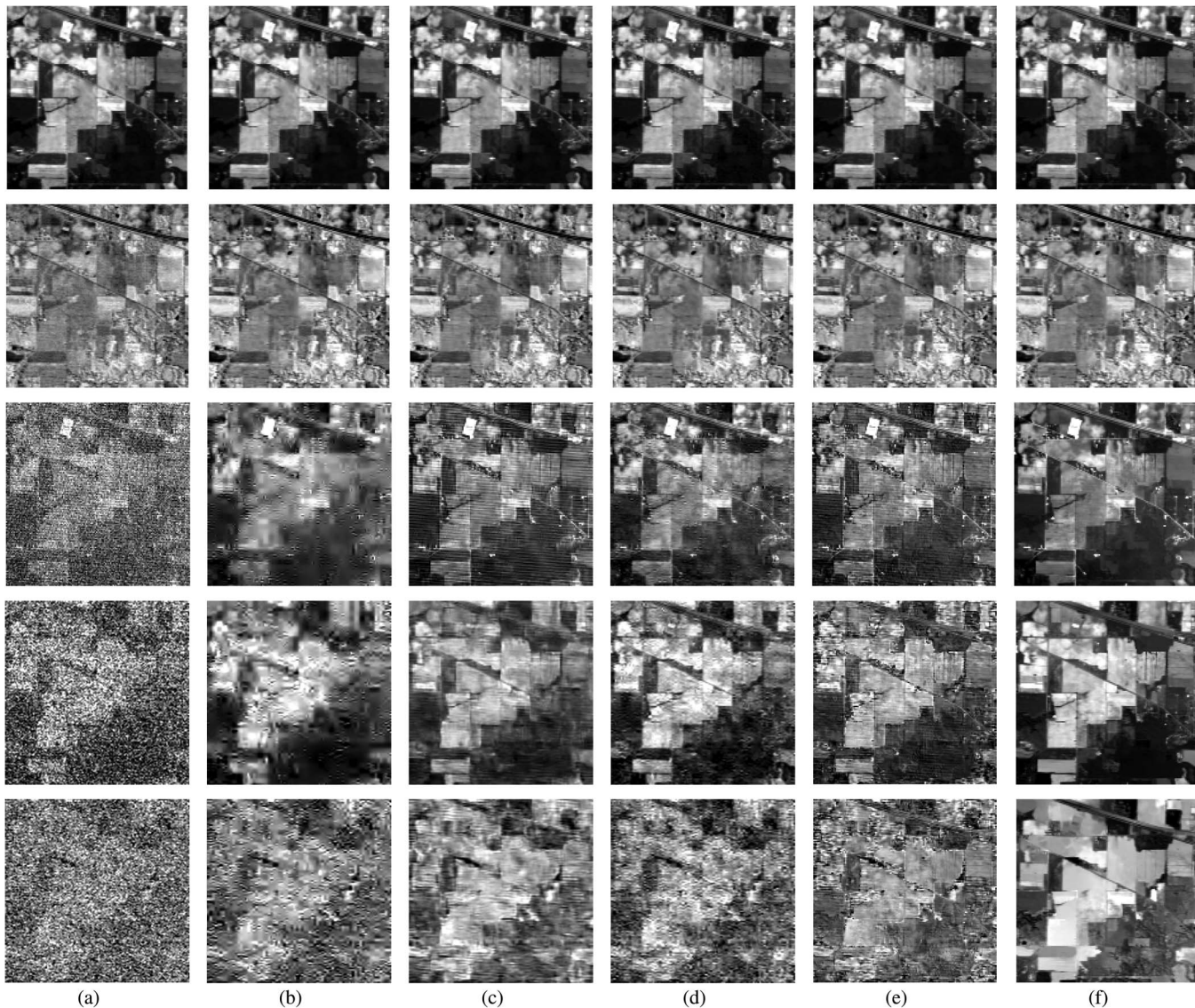


Fig. 9. Denoising results of different spectral bands in the data set of AVIRIS Indian Pines. From top to bottom, the images are the 25th, 79th, 1st, 163rd, and 108th spectral bands, respectively. (a) Original spectral bands. (b) Wavelet-bishrink [12]. (c) BM4D [23]. (d) PCA-wavelet [24]. (e) SASR. (f) SSASR.

regions and preserving structures, as shown in the first and second rows in Fig. 9. When it comes to the cases of more serious noise (e.g., the 1st, 108th, and 163rd spectral bands), more obvious superiority in noise removal and detail preservation can be seen from the results by the proposed SSASR method. Specifically, it can be seen that the wavelet-bishrink method fails in recovering important details. By keeping the important PCA component that represents structural information, the PCA-wavelet method can effectively preserve the details in the denoised 1st and 163rd spectral bands, while artifacts can be clearly observed. The BM4D method cannot avoid obvious striping and blurring effects in Fig. 9(c), whereas remained noise and striping effect can be observed in the SASR-based results in Fig. 9(e). In addition, the PCA-wavelet, BM4D, and SASR methods fail in restoring the 108th spectral band, which is corrupted with very strong noise. Based on the visual comparison in Figs. 8 and 9, the proposed SSASR method provides a more pleasant visual impression (much clearer and sharper edges) after the denoising processing. Even in the existence of very serious noise, the proposed SSASR method can restore the details effectively without introducing obvious artifacts.

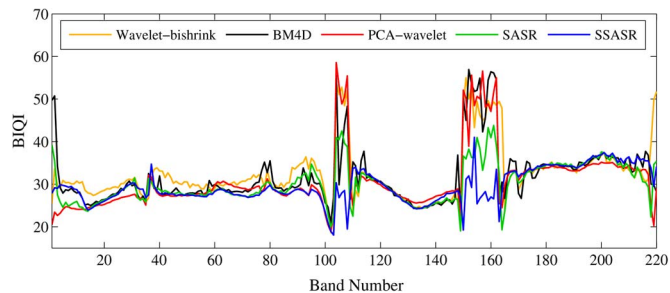


Fig. 10. Band-by-band BIQI of denoised results by different HSI denoising methods, with the data set of AVIRIS Indian Pines.

Since no noise-free ground reference images are available, the blind image quality index (BIQI) [49] is introduced to evaluate the image quality of each denoised spectral band. Generally, the lower the BIQI value is, the better quality the image has. Fig. 10 shows the band-by-band BIQI values of the denoised spectral bands by the different methods in comparison. In terms of the BIQI, it is clear that the BM4D, PCA-wavelet, and SASR methods are competitive in denoising some spectral bands, e.g., the 20th–30th and 180th–200th spectral bands,

TABLE IV
CLASSIFICATION ACCURACIES (%) WITH RANDOMLY SELECTED TRAINING SAMPLES
FOR AVIRIS INDIAN PINES DENOISED BY DIFFERENT DENOISING METHODS

Class	Train	Test	Noisy data set	Wavelet-bishrink [12]	BM4D [23]	PCA-wavelet [24]	SASR	SSASR
Alfalfa	6	48	64.46	96.28	95.95	93.01	97.92	100
Corn_N	144	1290	66.92	86.30	89.57	83.22	88.29	95.77
Corn_M	84	750	69.12	86.89	90.43	85.06	85.12	96.11
Corn	24	210	58.73	78.17	84.17	70.44	79.65	89.98
Grass_P	50	447	87.19	93.19	93.48	92.46	89.85	96.16
Grass_T	75	672	81.88	94.66	95.74	93.83	94.64	97.81
Grass_PM	3	23	76.00	96.93	98.65	97.03	99.07	99.20
Hay_W	49	440	87.93	95.58	98.23	97.41	97.68	98.84
Oats	2	18	20.00	91.38	91.46	68.91	76.73	99.47
Soybean_N	97	871	71.41	88.19	90.67	85.45	91.37	93.17
Soybean_M	247	2221	73.49	89.51	91.88	87.26	89.87	96.92
Soybean_C	62	552	64.71	84.25	86.14	84.25	82.56	94.66
Wheat	22	190	88.36	97.76	97.06	96.85	97.18	99.89
Woods	130	1164	91.17	96.48	98.41	94.59	97.57	99.67
Buildings	38	342	67.61	89.32	90.33	81.19	89.63	97.45
Stone	10	85	98.36	98.88	98.86	96.74	99.13	98.77
OA	-	-	75.93	90.12	92.39	87.94	90.66	96.57
AA	-	-	72.96	91.49	93.19	87.98	91.02	97.12
κ	-	-	0.724	0.887	0.913	0.862	0.893	0.961

when compared with the SSASR method. This is because some spectral bands are very slightly noisy and even noiseless, and both the compared methods and the proposed SSASR method are effective in removing slight noise and preserving the details in these spectral bands. When it comes to the serious noise, a great advantage can be observed in dealing with the majority of the 100th–110th and 150th–170th spectral bands by the proposed method. Overall, although the proposed SSASR method cannot guarantee an absolute advantage in dealing with all the spectral bands in terms of BIQI, the competitive performance in dealing with slight noise and the much better performance in recovering details in seriously noisy spectral bands demonstrate the overall merit of the proposed method. In addition, by calculating the mean value of BIQI (MBIQI) values in all the spectral bands, the corresponding MBIQI values are as follows: wavelet-bishrink MBIQI = 32.47, BM4D MBIQI = 31.87, PCA-wavelet MBIQI = 30.77, SASR MBIQI = 30.17, and SSASR MBIQI = 29.53, respectively. The lowest MBIQI is obtained by the proposed SSASR method, indicating that a better overall image quality can be obtained by the proposed method than the other three HSI denoising methods in comparison.

Furthermore, the classification results before and after denoising for the tested HSI are given in Table IV. Table IV demonstrates the effectiveness of the proposed SSASR-based HSI denoising method and objectively compares the different HSI denoising methods. As shown in Table IV, the AVIRIS Indian Pines data contain 16 classes of objects, where the reference map can be obtained from [3]. To accomplish supervised classification using the support vector machine (SVM)-based classification method [50], we randomly choose around 10% of the labeled samples for training and use the rest of the samples for testing. The classification is repeated ten times, and the mean values are noted as the final classification assessment results. In Table IV, the indexes of classification accuracy for each class, the overall accuracy (OA), the average accuracy (AA), and the κ coefficient measure are given. It is clear that the traditional SVM classification method is greatly affected

by the varying degrees of noise across bands, with the OA, AA, and κ coefficients being 75.93%, 72.96%, and 0.724, respectively. However, by operating the SVM classifier on the denoised hypercube, the classification accuracies are obviously increased. It can be seen from Table IV that the proposed SSASR approach shows the highest classification accuracies, i.e., OA 96.57%, AA 97.12%, and κ 0.961. In terms of class-specific classification results, the proposed SSASR method has the best classification accuracies for 15 of the 16 classes, which are shown in bold in Table IV. In summary, the superior classification accuracy obtained by the SSASR method demonstrates the advantage of the proposed method, which will contribute to its usefulness in future practical surveillance and analysis missions.

E. Analysis of Computational Complexity

There are three main stages in the proposed method: spectral-adaptive band-subset partition, spatial-adaptive local similar pixel searching, and SR-based noise-free estimation. The third stage is the most time consuming part mainly because of two loops (the pixel-by-pixel processing and the iterated update for noise-free estimation). In the inner loop of pixelwise processing, there are two main calculations. The first one is denoted by (10), which is the SVD-based matrix decomposition. Fundamentally, the SVD is an $O(pq \cdot \min(p, q))$ -complexity problem [51], where p and q represent the row and column of the sparse matrix \mathbf{Y}_i , respectively. Another one is mathematically denoted in (11) and (12), where $S_\tau(\Sigma_i)$ is a diagonal matrix with size of $r \times r$, $r \leq \min(p, q)$; therefore, the time complexity of the matrix multiplication in (11) and (12) is $O(pq \cdot r)$. Considering the time complexity of (10)–(12), the overall computational complexity of the inner loop should be $O(pq \cdot \min(p, q))$. Let T_{iter} denote the number of iteration time and $M \times N$ the size of each spectral band; then, the computational complexity of the proposed SSASR method is $O(T_{\text{iter}} \cdot MN \cdot pq \cdot \min(p, q))$. Because the sparse coding on each matrix \mathbf{Y}_i is independent from each other, the pixel-by-pixel processing can be replaced

by parallel processing, which can result in the reduced computational complexity of $O(T_{\text{iter}} \cdot pq \cdot \min(p, q))$.

V. CONCLUSION

In this paper, a novel SSASR method has been proposed for denoising the HSI. First, with the proposed spectral-adaptive band-subset partition and spatial-adaptive local similar pixel searching schemes, spectral-spatial similar pixels can be effectively searched and grouped. Second, noise-free estimations for each group of spectral pixels with highly spectral-spatial similarity are generated by solving a joint SR-based optimization problem. By making full use of highly correlated spectral information and highly similar spatial information in HSI via the SR, the proposed method achieves excellent denoising performance in terms of overall image quality improvement and structure/spectral characteristics preservation, which can be demonstrated in both simulated and real experiments. When compared with different HSI denoising methods, including the band-by-band wavelet-shrinkage, BM4D, and PCA-wavelet methods, the proposed SSASR method demonstrates superiority both numerically and visually.

In addition, it should be noted that the proposed SSASR method focused on Gaussian noise. Extending it to be more appropriate to deal with the other forms of noise in HSI, e.g., non-Gaussian distributed noise, impulse noise, and stripping noise, is the focus of future work. In addition, due to atmosphere effects and the intrinsic sensor problem, the information in some bands of HSIs may be lost. Thus, another research topic is to do work on junk band restoration based on the findings of this paper.

ACKNOWLEDGMENT

The authors would like to thank Prof. D. Landgrebe from Purdue University and the National Aeronautics and Space Administration Jet Propulsion Laboratory for providing the free downloads of the hyperspectral data sets. They would also like to thank Dr. M. Maggioni for providing the code of the BM4D filter and the editors and anonymous reviewers for their insightful comments and suggestions, which have greatly improved this paper.

REFERENCES

- [1] W. Li, S. Prasad, J. Fowler, and L. Bruce, "Locality-preserving dimensionality reduction and classification for hyperspectral image analysis," *IEEE Trans. Geosci. Remote Sens.*, vol. 50, no. 4, pp. 1185–1198, Apr. 2012.
- [2] J. Li, J. Dias, and A. Plaza, "Spectral-spatial hyperspectral image segmentation using subspace multinomial logistic regression and markov random fields," *IEEE Trans. Geosci. Remote Sens.*, vol. 50, no. 3, pp. 809–823, Mar. 2012.
- [3] L. Zhang, D. Tao, and X. Huang, "On combining multiple features for hyperspectral remote sensing image classification," *IEEE Trans. Geosci. Remote Sens.*, vol. 50, no. 3, pp. 879–893, Mar. 2012.
- [4] E. Christophe, D. Leger, and C. Mailhes, "Quality criteria benchmark for hyperspectral imagery," *IEEE Trans. Geosci. Remote Sens.*, vol. 43, no. 9, pp. 2103–2114, Sep. 2005.
- [5] N. Acito, M. Diani, and G. Corsini, "Signal-dependent noise modeling and model parameter estimation in hyperspectral images," *IEEE Trans. Geosci. Remote Sens.*, vol. 49, no. 8, pp. 2957–2971, Aug. 2011.
- [6] T. Lin and S. Bourennane, "Hyperspectral image processing by jointly filtering wavelet component tensor," *IEEE Trans. Geosci. Remote Sens.*, vol. 51, no. 6, pp. 3529–3541, Jun. 2013.
- [7] Q. Yuan, L. Zhang, and H. Shen, "Hyperspectral image denoising employing a spectral-spatial adaptive total variation model," *IEEE Trans. Geosci. Remote Sens.*, vol. 50, no. 10, pp. 3660–3677, Oct. 2012.
- [8] X. Liu, S. Bourennane, and C. Fossati, "Denoising of hyperspectral images using the PARAFAC model and statistical performance analysis," *IEEE Trans. Geosci. Remote Sens.*, vol. 50, no. 10, pp. 3717–3724, Oct. 2012.
- [9] B. Rasti, J. Sveinsson, and M. Ulfarsson, "Wavelet-based sparse reduced-rank regression for hyperspectral image restoration," *IEEE Trans. Geosci. Remote Sens.*, vol. 52, no. 10, pp. 6688–6698, Oct. 2014.
- [10] Y. Zhao and J. Yang, "Hyperspectral image denoising via sparse representation and low-rank constraint," *IEEE Trans. Geosci. Remote Sens.*, vol. 57, no. 1, pp. 296–308, Jan. 2015.
- [11] Y. Kopsinis and S. McLaughlin, "Development of EMD-based denoising methods inspired by wavelet thresholding," *IEEE Trans. Signal Process.*, vol. 57, no. 4, pp. 1351–1362, Apr. 2009.
- [12] "Matlab Implementation of Wavelet Transforms," Electr. Eng. Polytechnic Univ., Brooklyn, NY, USA. [Online]. Available: <http://eeeweb.poly.edu/iselesni/WaveletSoftware/index.html>
- [13] Y. Wen, M. Ng, and Y. Huang, "Efficient total variation minimization methods for color image restoration," *IEEE Trans. Image Process.*, vol. 17, no. 11, pp. 2081–2088, Nov. 2008.
- [14] T. Goldstein and S. Osher, "The split Bregman method for L1-regularized problems," *SIAM J. Imaging Sci.*, vol. 2, no. 2, pp. 323–343, Apr. 2009.
- [15] D. Letexier and S. Bourennane, "Noise removal from hyperspectral images by multidimensional filtering," *IEEE Trans. Geosci. Remote Sens.*, vol. 46, no. 7, pp. 2061–2069, Jul. 2008.
- [16] A. Karami, M. Yazdi, and A. Asli, "Noise reduction of hyperspectral images using kernel non-negative Tucker decomposition," *IEEE J. Sel. Topics Signal Process.*, vol. 5, no. 3, pp. 487–493, Jun. 2011.
- [17] S. Bourennane, C. Fossati, and A. Cailly, "Improvement of target detection algorithms based on adaptive 3-D filtering," *IEEE Trans. Geosci. Remote Sens.*, vol. 49, no. 4, pp. 1383–1395, Apr. 2011.
- [18] P. Zhong and R. Wang, "Multiple-spectral-band CRFs for denoising junk bands of hyperspectral imagery," *IEEE Trans. Geosci. Remote Sens.*, vol. 51, no. 4, pp. 2260–2275, Apr. 2013.
- [19] T. Lin and S. Bourennane, "Survey of hyperspectral image denoising methods based on tensor decompositions," *EURASIP J. Adv. Signal Process.*, vol. 2013, no. 1, pp. 1–11, Dec. 2013.
- [20] A. Buades, B. Coll, and J. Morel, "A non-local algorithm for image denoising," in *Proc. IEEE Conf. Comput. Vis. Pattern Recog.*, San Diego, CA, USA, Jun. 2005, vol. 2, pp. 60–65.
- [21] Y. Qian and M. Ye, "Hyperspectral imagery restoration using nonlocal spectral-spatial structured sparse representation with noise estimation," *IEEE J. Sel. Topics Appl. Earth Observ. Remote Sens.*, vol. 6, no. 2, pp. 499–515, Apr. 2013.
- [22] K. Dabov, A. Foi, and K. Egiazarian, "Video denoising by sparse 3-D transform-domain collaborative filtering," in *Proc. 15th Eur. Signal Process. Conf.*, Poznan, Poland, Sep. 2007, vol. 1, pp. 27–35.
- [23] M. Maggioni, V. Katkovnik, K. Egiazarian, and A. Foi, "A nonlocal transform-domain filter for volumetric data denoising and reconstruction," *IEEE Trans. Image Process.*, vol. 22, no. 1, pp. 119–133, Jan. 2013.
- [24] G. Chen and S. Qian, "Denoising of hyperspectral imagery using principal component analysis and wavelet shrinkage," *IEEE Trans. Geosci. Remote Sens.*, vol. 49, no. 3, pp. 973–980, Mar. 2011.
- [25] L. Sendur and I. Selesnick, "Bivariate shrinkage with local variance estimation," *IEEE Signal Process. Lett.*, vol. 9, no. 12, pp. 438–441, Dec. 2002.
- [26] I. Selesnick, R. Baraniuk, and N. Kingsbury, "The dual-tree complex wavelet transform," *IEEE Signal Process. Mag.*, vol. 22, no. 6, pp. 123–151, Nov. 2005.
- [27] Q. Yuan, L. Zhang, and H. Shen, "Hyperspectral image denoising with a spatial-spectral view fusion strategy," *IEEE Trans. Geosci. Remote Sens.*, vol. 52, no. 5, pp. 2314–2325, May 2014.
- [28] X. Zhu and P. Milanfar, "Automatic parameter selection for denoising algorithms using a no-reference measure of image content," *IEEE Trans. Image Process.*, vol. 19, no. 12, pp. 3116–3132, Dec. 2010.
- [29] H. Othman and S. Qian, "Noise reduction of hyperspectral imagery using hybrid spatial-spectral derivative-domain wavelet shrinkage," *IEEE Trans. Geosci. Remote Sens.*, vol. 44, no. 2, pp. 397–408, Feb. 2006.
- [30] Z. Xing, M. Zhou, A. Castrodad, G. Sapiro, and L. Carin, "Dictionary learning for noisy and incomplete hyperspectral images," *SIAM J. Imaging Sci.*, vol. 5, no. 1, pp. 33–56, Jan. 2012.
- [31] M. Ye, Y. Qian, and J. Zhou, "Multitask sparse nonnegative matrix factorization for joint spectral-spatial hyperspectral imagery denoising," *IEEE Trans. Geosci. Remote Sens.*, vol. 53, no. 5, pp. 2621–2639, May 2015.
- [32] H. Zhang, W. He, L. Zhang, H. Shen, and Q. Yuan, "Hyperspectral image restoration using low-rank matrix recovery," *IEEE Trans. Geosci. Remote Sens.*, vol. 52, no. 8, pp. 4729–4743, Aug. 2014.
- [33] W. He, H. Zhang, L. Zhang, and H. Shen, "Hyperspectral image denoising via noise-adjusted iterative low-rank matrix approximation," *IEEE J. Sel. Topics Appl. Earth Observ. Remote Sens.*, to be published.
- [34] M. Elad and M. Aharon, "Image denoising via sparse and redundant representations over learned dictionaries," *IEEE Trans. Image Process.*, vol. 15, no. 12, pp. 3736–3745, Dec. 2006.
- [35] A. Bruckstein, D. Donoho, and M. Elad, "From sparse solutions of systems of equations to sparse modeling of signals and images," *SIAM Rev.*, vol. 51, no. 1, pp. 34–81, Feb. 2009.

- [36] J. Mairal, F. Bach, J. Ponce, G. Sapiro, and A. Zisserman, "Non-local sparse models for image restoration," in *Proc. IEEE Int. Conf. Comput. Vis.*, Kyoto, Japan, Sep. 2009, pp. 2272–2279.
- [37] D. Donoho, "Denoising by soft-thresholding," *IEEE Trans. Inf. Theory*, vol. 41, no. 3, pp. 613–627, May 1995.
- [38] A. Foi, V. Katkovnik, and K. Egiazarian, "Pointwise shape-adaptive DCT for high-quality denoising and deblurring of grayscale and color images," *IEEE Trans. Image Process.*, vol. 16, no. 5, pp. 1395–1411, May 2007.
- [39] J. Fan and I. Gijbels, *Local Polynomial Modelling and Its Application*. London, U.K.: Chapman & Hall, 1996.
- [40] V. Katkovnik, K. Egiazarian, and J. Astola, *Local Approximation Techniques in Signal and Image Processing*. Bellingham, WA, USA: SPIE, 2006.
- [41] W. Dong, G. Shi, and X. Li, "Nonlocal image restoration with bilateral variance estimation: A low-rank approach," *IEEE Trans. Image Process.*, vol. 22, no. 2, pp. 700–711, Feb. 2013.
- [42] S. Osher, M. Burger, D. Goldfarb, J. Xu, and W. Yin, "An iterative regularization method for total variation-based image restoration," *Multiscale Model. Simul.*, vol. 4, no. 2, pp. 460–489, Jul. 2006.
- [43] J. Xu and S. Osher, "Iterative regularization and nonlinear inverse scale space applied to wavelet-based denoising," *IEEE Trans. Image Process.*, vol. 16, no. 2, pp. 534–544, Feb. 2007.
- [44] Hyperspectral Images. [Online]. Available: <http://engineering.purdue.edu/~biehl/MultiSpec/hyperspectral.html>
- [45] Hyperspectral Images. [Online]. Available: <http://aviris.jpl.nasa.gov/html/aviris.freedata.html>
- [46] M. Iordache, J. Dias, and A. Plaza, "Collaborative sparse regression for hyperspectral unmixing," *IEEE Trans. Geosci. Remote Sens.*, vol. 52, no. 1, pp. 341–354, Jan. 2014.
- [47] Z. Wang, A. Bovik, and H. Sheikh, "Image quality assessment: From error visibility to structural similarity," *IEEE Trans. Image Process.*, vol. 13, no. 4, pp. 600–612, Apr. 2004.
- [48] J. Chen, X. Jia, W. Yang, and B. Matsushita, "Generalization of subpixel analysis for hyperspectral data with flexibility in spectral similarity measures," *IEEE Trans. Geosci. Remote Sens.*, vol. 47, no. 7, pp. 2165–2171, Jul. 2009.
- [49] A. Moorthy and A. Bovik, "A two-step framework for constructing blind image quality indices," *IEEE Signal Process. Lett.*, vol. 17, no. 5, pp. 513–516, May 2010.
- [50] Support Vector Machine Based Classification. [Online]. Available: <http://www.csie.ntu.edu.tw/~cjlin/libsvm/>
- [51] M. Brand, "Fast low-rank modifications of the thin singular value decomposition," *Linear Algebra Appl.*, vol. 415, no. 1, pp. 20–30, May 2006.



Ting Lu received the B.Sc. degree from Hunan University, Changsha, China, in 2011. She is currently working toward the Ph.D. degree at Hunan University.

From September 2014 to September 2015, she was a Visiting Ph.D. Student with the Department of Information Engineering and Computer Science, University of Trento, Trento, Italy, supported by the China Scholarship Council. Her research interests include sparse representation and remote sensing image processing.

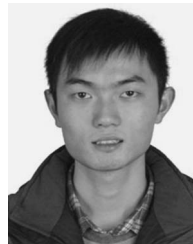


Shutao Li (M'07–SM'15) received the B.S., M.S., and Ph.D. degrees from Hunan University, Changsha, China, in 1995, 1997, and 2001, respectively, all in electrical engineering.

In 2001, he joined the College of Electrical and Information Engineering, Hunan University, where he is currently a Full Professor. From May 2001 to October 2001, he was a Research Associate with the Department of Computer Science, The Hong Kong University of Science and Technology, Hong Kong. From November 2002 to November 2003, he was a

Postdoctoral Fellow with the Royal Holloway College, University of London, Surrey, U.K., working with Prof. John Shawe-Taylor. During April 2005 to June 2005, he was a Visiting Professor with the Department of Computer Science, The Hong Kong University of Science and Technology. He has authored or coauthored over 160 refereed papers. His professional interests are compressive sensing, sparse representation, image processing, and pattern recognition.

Dr. Li is an Associate Editor of the IEEE TRANSACTIONS ON GEOSCIENCE AND REMOTE SENSING and a member of the Editorial Board of the journals Information Fusion and Sensing and Imaging. He was a recipient of two second-grade national awards at the Science and Technology Progress of China in 2004 and 2006.



Leyuan Fang (S'10–M'14) received the Ph.D. degree in electrical engineering from Hunan University, Changsha, China, in 2015.

From September 2011 to September 2012, he was a Visiting Ph.D. Student with the Department of Ophthalmology, Duke University, Durham, NC, USA, supported by the China Scholarship Council. Since June 2013, he has been an Assistant Professor with the College of Electrical and Information Engineering, Hunan University. His research interests include sparse representation and multiresolution

analysis in remote sensing and medical image processing.

Dr. Fang was a recipient of the Scholarship Award for Excellent Doctoral Student granted by the Chinese Ministry of Education in 2011.



Yi Ma received the Ph.D. degree in physical oceanography from the Chinese Academy of Sciences, Beijing, China, in 2005.

In 2000, he joined the First Institute of Oceanography, State Oceanic Administration, where he is currently a Research Professor with the division of marine physics and remote sensing. During November 2005 to January 2006, he was a Visiting Professor with the Malaysia Center of Remote Sensing. His professional interests are hyperspectral remote sensing, wetland monitoring, and remote

sensing bathymetry.

Dr. Ma is the Deputy Secretary General of the Committee on the Remote Sensing of China Marine Society, Chinese Society of Oceanology and Limnology. He was a recipient of the First-Grade Marine Science and Technology Award of China in 2015.



Jón Atli Benediktsson (S'84–M'90–SM'99–F'04) received the Cand.Sci. degree from the University of Iceland, Reykjavik, Iceland, in 1984 and the M.S.E.E. and Ph.D. degrees from Purdue University, West Lafayette, IN, USA, in 1987 and 1990, respectively, all in electrical engineering.

On July 1, 2015, he became the Rector of the University of Iceland, where he was the Pro Rector of Science and Academic Affairs and a Professor of electrical and computer engineering from 2009 to 2015. He is a Cofounder of the biomedical start-up

company Oxymap. His research interests are in remote sensing, image analysis, pattern recognition, biomedical analysis of signals, and signal processing. He has published extensively in those fields.

Prof. Benediktsson is a Fellow of The International Society for Optics and Photonics. He is a member of the 2014 IEEE Fellow Committee. He was the 2011–2012 President of the IEEE Geoscience and Remote Sensing Society (GRSS) and has been on the GRSS Administrative Committee since 2000. He is on the Editorial Board of the PROCEEDINGS OF THE IEEE and the International Editorial Board of the *International Journal of Image and Data Fusion*. He was the Editor-in-Chief of the IEEE TRANSACTIONS ON GEOSCIENCE AND REMOTE SENSING (TGRS) from 2003 to 2008. He has served as an Associate Editor of TGRS since 1999, the IEEE GEOSCIENCE AND REMOTE SENSING LETTERS since 2003, and IEEE ACCESS since 2013. He was the Chairman of the Steering Committee of the IEEE JOURNAL OF SELECTED TOPICS IN APPLIED EARTH OBSERVATIONS AND REMOTE SENSING in 2007–2010. He was a recipient of the Stevan J. Kristof Award from Purdue University in 1991 as an outstanding graduate student in remote sensing. He was the recipient of the Icelandic Research Council's Outstanding Young Researcher Award in 1997, was granted the IEEE Third Millennium Medal in 2000, was a corecipient of the University of Iceland's Technology Innovation Award in 2004, and was a recipient of the yearly research award from the Engineering Research Institute of the University of Iceland in 2006 and the Outstanding Service Award from the IEEE GRSS in 2007. He was corecipient of the IEEE TGRS Paper Award in 2012 and the IEEE GRSS Highest Impact Paper Award in 2013. He was a recipient of the IEEE/VFI Electrical Engineer of the Year Award in 2013 and was a corecipient of the International Journal of Image and Data Fusion Best Paper Award in 2014. He is also a member of the Association of Chartered Engineers in Iceland (VFI), Societas Scinetiarum Islandica, and Tau Beta Pi.